



Double-confined nanoheterostructure Sb/Sb₂S₃@Ti₃C₂T_x@C toward ultra-stable Li-/Na-ion batteries

Dan Wang, Qun Ma, Huan He, Zhi-Yuan Wang* , Run-Guo Zheng, Hong-Yu Sun, Yan-Guo Liu, Chun-Li Liu

Received: 28 April 2023 / Revised: 10 July 2023 / Accepted: 11 July 2023 / Published online: 29 January 2024
© Youke Publishing Co., Ltd. 2024

Abstract Antimony-based materials with high capacities and moderate potentials are promising anodes for lithium-/sodium-ion batteries. However, their tremendous volume expansion and inferior conductivity lead to poor structural stability and sluggish reaction kinetics. Herein, a double-confined nanoheterostructure Sb/Sb₂S₃@Ti₃C₂T_x@C has been fabricated through a solvothermal method followed by low-temperature heat treatment. The dual protection of “MXene” and “carbon” can better accommodate the volume expansion of Sb/Sb₂S₃. The strong covalent bond (Ti–S, Ti–O–Sb, C–O–Sb) can firmly integrate Sb-based material with Ti₃C₂T_x and carbon, which significantly improves the structure stability. In addition, the carbon layer can restrain the oxidation of MXenes, and the nano-Sb/Sb₂S₃ can facilitate electron/ion transport and suppress the restacking of MXenes. The heterogeneous interface between Sb and Sb₂S₃ can

further promote interfacial charge transfer. The MXene-Sb/Sb₂S₃@C-1 with the optimal Sb content shows high specific capacities, comparable rate properties and ultra-stable cycling performances (250 mAh·g⁻¹ after 2500 cycles at 1 A·g⁻¹ for sodium-ion batteries). Ex situ X-ray diffractometer (XRD) test reveals the storage mechanism including the conversion and alloying process of MXene-Sb/Sb₂S₃@C-1. Cyclic voltammetry (CV) test results demonstrate that the pseudo-capacitance behavior is dominant in MXene-Sb/Sb₂S₃@C-1, especially at large current. This design paves the way for exploring high-performance alloy-based/conversion-type anode for energy storage devices.

Keywords Sb/Sb₂S₃; MXene; Carbon; Anode; Lithium-ion batteries; Sodium-ion batteries

Supplementary Information The online version contains supplementary material available at <https://doi.org/10.1007/s12598-023-02550-3>.

D. Wang, Q. Ma, H. He, Z.-Y. Wang*, R.-G. Zheng, Y.-G. Liu
School of Materials Science and Engineering, Northeastern University, Shenyang 110819, China
e-mail: zhiyuanwang@neuq.edu.cn

D. Wang, Q. Ma, H. He, Z.-Y. Wang, R.-G. Zheng, H.-Y. Sun, Y.-G. Liu
School of Resources and Materials, Northeastern University at Qinhuangdao, Qinhuangdao 066004, China

D. Wang, Z.-Y. Wang, R.-G. Zheng, Y.-G. Liu
Key Laboratory of Dielectric and Electrolyte Functional Material Hebei Province, Qinhuangdao 066004, China

C.-L. Liu
Department of Physics and Oxide Research Center, Hankuk University of Foreign Studies, Yongin 17035, Korea

1 Introduction

The rapid development of science and technology strongly relies on the support of energy. During the past decades, lithium-ion batteries (LIBs) have been widely applied in multiple fields as important energy storage devices due to their advantages of high energy density, high power density as well as high security. In recent years, due to the limited reserves and uneven distribution of lithium resources, exploring new energy techniques is urgently needed. Sodium-ion batteries (SIBs) have become one of the most popular candidates by virtue of their high natural abundance and low cost of Na, as well as the similar storage mechanism to LIBs [1]. However, the larger ionic radius of Na⁺ (0.102 nm) compared with Li⁺ (0.059 nm) generally leads to slow reaction kinetics and unsatisfied electrochemical performances [2]. In this case, it is challenging but desirable to explore suitable electrode materials with high performance for SIBs.



To date, numerous potential anode materials have been investigated, such as carbonaceous materials [3], alloy-based compounds [4], transition metal oxides [5], phosphides [6] and sulfides [7]. Among them, Sb-based materials with high capacities have attracted great attention, including Sb, Sb-based alloys, Sb_2O_3 , Sb_2O_4 and Sb_2S_3 [8]. In particular, antimony trisulfide (Sb_2S_3), which is based on multielectron conversion/alloy reactions, shows attractive theoretical capacity ($947 \text{ mAh}\cdot\text{g}^{-1}$), great thermal stability, abundant resource, popular price and better reversibility compared to oxides [9]. However, the problem of serious volume expansion and poor conductivity still exists in Sb_2S_3 , which may lead to active material pulverization and slow charge transport, resulting in an inferior cycle and rate performance. Designing nanostructure and combining Sb_2S_3 with protective substance, which can reduce stress, relieve volume effect and improve conductivity effectively, are two common optimization approaches to address the above issues [10, 11]. In addition, a new method of fabricating heterostructure composite has been put forward recently [12]. The heterostructures with different phase compositions can effectively relieve internal pressure and promote interfacial charge transfer. For instance, Zhang et al. [13] fabricated $\text{Sb}_2\text{S}_3/\text{MoS}_2$ composite, which exhibited better electrochemical properties in SIBs compared with individual Sb_2S_3 and MoS_2 nanomaterials. Jia and co-workers [14] synthesized hierarchical $\text{Sb}_2\text{S}_3/\text{SnS}_2/\text{C}$ and found that the heterogeneous structure led to a built-in electric field, which decreased ion diffusion resistance and promoted ion and electron transport. $\text{CoS}_2/\text{Sb}_2\text{S}_3$ nanocrystals encapsulated into a dual-carbon framework was reported by Li's group [15], and an excellent sodium storage performance was obtained by the synergistic effect of the heterostructure. Moreover, Ke's group [16] designed $\text{Sb}_2\text{S}_3\text{-Co}_9\text{S}_8/\text{NC}$ heterogeneous material, which exhibited excellent cycle stability as well as fast lithium-ion transfer kinetics. Dong et al. [17] developed $\text{ZnS-Sb}_2\text{S}_3/\text{C}$ core-double-shell material and obtained $630 \text{ mAh}\cdot\text{g}^{-1}$ at $100 \text{ mA}\cdot\text{g}^{-1}$ after 120 cycles in SIBs due to the improved electrochemical reaction kinetics and structure stability.

Although obvious improvements in electrochemical performance have been obtained in heterogeneous structure composites, most of the reported materials are consisted of two kinds of "sulfides", which all have huge volume change and extremely low conductivity. To further optimize the performance of Sb_2S_3 , incorporating alloy-type metallic Sb with sulfides seems to be a wise choice. Li et al. [18] synthesized $\text{Sb@Sb}_2\text{S}_3/\text{C}$, benefiting from the robust skeleton frameworks and high electronic conductivity from amorphous carbon nanotubes and metallic Sb, the anode exhibited a high specific capacity of $1596 \text{ mAh}\cdot\text{g}^{-1}$ at $0.1 \text{ A}\cdot\text{g}^{-1}$ and stable cycling performance in LIBs. Wu and his group [19] prepared Sb/

$\text{Sb}_2\text{S}_3/\text{C}$, which exhibited excellent potassium-ion storage performance. These reports indicate that it is worth further investigating the combination of Sb and Sb_2S_3 because it is promising in achieving effective enhancement in the electrochemical performance.

In addition, the introduction of conductive matrixes is also significant for Sb-based materials to alleviate the volume expansion and increase conductivity, while most of the reported matrixes are carbonaceous materials at present. The nonpolar nature and the limited defect sites of carbon may lead to weak interface bonding force between active material and carbon, which results in an unstable interface and inefficient contact. The limited theoretical capacity of carbon may also bring a loss in the specific capacity of the whole composite. On this point, MXene (transition metal carbide or nitride), a new type of two-dimensional material, can be a better choice. Owing to the ultra-high conductivity ($10^4 \text{ S}\cdot\text{cm}^{-1}$), excellent mechanical strength and hydrophilicity, low-diffusion-energy barrier and abundant reaction sites, MXenes have been extensively investigated in energy storage devices such as alkali metal-ion batteries and supercapacitors [20]. As a typical representative, $\text{Ti}_3\text{C}_2\text{T}_x$ has a high theoretical capacity of $352 \text{ mAh}\cdot\text{g}^{-1}$ as the anode in SIBs. The rich terminal groups T (O-, OH- and F-) on the surface of $\text{Ti}_3\text{C}_2\text{T}_x$ can induce a strong binding affinity to metal-based materials, which is beneficial for forming robust interfaces [21–28]. However, the restacking issue of pure MXene nanosheets affects the achievable sites for reversible charge/discharge, so it shows limited capacity when used as an electrode alone. And MXenes are commonly easy to be oxidized under a violent environment.

Based on the current situation, in this work, we integrated nanoengineering, heterogeneous structure design and stable conductive network together, to construct a kind of MXene/carbon double-confined $\text{Sb/Sb}_2\text{S}_3$ nanoheterostructure by a facile and highly effective one-step solvothermal followed by annealing process. The in situ formed nanoparticles of Sb and Sb_2S_3 can be homogeneously anchored on the $\text{Ti}_3\text{C}_2\text{T}_x$ nanosheets covered by ultra-thin conductive carbon networks, and the grain growth of Sb-based materials can be well confined to avoid excessive particle size. The MXene with abundant functional groups not only serves as a flexible conductive matrix to buffer the volume change and accelerate the electron transfer but also improves the structure stability by establishing a solid interface through strong covalent bonding of Ti–O–Sb and S–Ti. The coated carbon network further enhances the electronic conductivity, promotes the charge transfer kinetics, buffers the volume expansion, maintains the structural integrity of the electrode and also protects $\text{Ti}_3\text{C}_2\text{T}_x$ from oxidation and avoiding the parasitic reaction between Sb-based active anode and electrolyte.

Furthermore, the heterogeneous interface of Sb₂S₃ and Sb can accelerate electron transport. The nanostructure is beneficial for both the efficient ion and electron transport and the wettability of electrolytes. In addition, the effect of the content of Sb-based materials on the morphology and performance was also investigated. Benefiting from the particular heterostructure and the synergistic effect between Sb-based heterogeneous nanostructure and carbon-coated MXene, the composite anode with the optimal Sb/Sb₂S₃ content delivers high charge/discharge capacities, excellent rate properties and ultra-stable cycle performances in SIBs and LIBs. The storage mechanism of the composite was revealed by *ex situ* X-ray diffraction (XRD). Cyclic voltammetry (CV) test proved that the pseudocapacitance behavior is dominant in the composite. This research puts forward simple and effective tactics to establish composite anode for highly efficient energy storage applications.

2 Experimental

2.1 Materials preparation

All the chemicals including LiF (99%), HCl (AR), ammonia solution (NH₃·H₂O, AR), SbCl₃ (AR), Sb (99%), glucose (C₆H₁₂O₆, AR) and thiourea (CH₄N₂S, ≥ 98%) were purchased from Aladdin Reagent Co., Ltd. The Ti₃AlC₂ (≥ 98%) powder was purchased from Foshan Xinxi Technology Co., Ltd.

2.2 Preparation of Ti₃C₂T_x

Firstly, 1.6 g LiF was dissolved in HCl solution (9.0 mol·L⁻¹, 20 ml) and stirred for 10 min. Then 1 g Ti₃AlC₂ powder was slowly added to the mixed solution and kept stirring for 24 h at 40 °C to etch. The mixture was washed with 1 mol·L⁻¹ HCl with a centrifuge to remove LiF, and then the mixture was washed with water until the pH of the supernatant reached 6. After that, the precipitate was added to deaerated water and sonicated for 2 h. At last, the solution was centrifuged for 60 min to separate a few-layer MXene. The concentration of the Ti₃C₂T_x MXene solution was 10.0 mg·ml⁻¹.

2.3 Preparation of Sb/Sb₂S₃@Ti₃C₂T_x@C composite

75 mg SbCl₃ and 5 ml Ti₃C₂T_x dispersion liquid were first added to 40 ml of ethylene glycol to thoroughly mix under stirring. And 0.5 ml HCl solution was added to the above solution to inhibit the hydrolysis of SbCl₃. After stirring for 24 h, 50 mg glucose and 1.5 mmol thiocarbamide was

added as carbon source and sulfur source and kept stirring for the other 2 h. Then the mixture was put in the Teflon-lined autoclave and kept at 160 °C for 12 h. After being washed with water by centrifuge several times, the precipitate was put in the freeze-drier to remove water. To completely carbonize the glucose and improve the crystallinity of the composite, the dried sample was calcined at 400 °C for 2 h and named as MX-Sb/Sb₂S₃@C-1. In addition, to investigate the effect of the load amount of Sb-based material on electrochemical performance, two other samples with different amounts of SbCl₃ (37.5/112.5 mg) were also prepared and named as MX-Sb/Sb₂S₃@C-0.5 and MX-Sb/Sb₂S₃@C-1.5, respectively. For comparison, pure Sb₂S₃ was also synthesized under the same treatment process.

2.4 Material characterization

The phase structures of the fabricated materials were characterized by X-ray diffraction (XRD, Rigaku SmartLab) with a copper target ($\lambda_{K\alpha} = 0.15406$ nm). The microstructure analysis was examined using field emission scanning electron microscopy (FESEM, ZEISS SUPRA55) and transmission electron microscopy (TEM, Talos F200X). Fourier transform infrared (FTIR) spectra were recorded on a spectrometer (Shimadzu FTIR-8400S) in ambient air at room temperature (25 °C). The surface element chemical valences of the materials were studied by X-ray photoelectron spectroscopy (XPS, Thermo Escalab 250XI). The specific surface areas and pore volumes of the samples were analyzed using N₂ adsorption through the Brunauer–Emmett–Teller (BET) equation. Element composition was determined by inductively coupled plasma optical emission spectrometer (ICP-OES, Agilent 5110).

2.5 Electrochemical characterizations

The anode was composed of 80 wt% as-prepared composite, 10 wt% conductive acetylene black, 10 wt% N-carboxymethyl cellulose (CMC) binder and deionized water as the solvent. Put the above slurry onto copper foil of 12 mm diameter and dry at 110 °C overnight. Coin cells (CR2032) were assembled in a glovebox with H₂O < 0.1 × 10⁻⁶ and O₂ < 0.1 × 10⁻⁶. For LIBs, the metal Li was used as the counter electrode and reference electrode. Monolayer polypropylene (Celgard2500) was used as the separator. LiPF₆ dissolved in a mixture of ethylene methyl carbonate (EMC), ethylene carbonate (EC) and dimethyl carbonate (DMC) with a volume ratio of 1:1:1 was used as the electrolyte. For SIBs, Whatman GF/C microfiber glass acts as the separator, and 1 mol·L⁻¹ NaClO₄ in 1:1 (weight ratio) EC/DEC with 5% fluoroethylene carbonate (FEC) additive acts as the electrolyte.

The electrochemical performance was measured by the LAND battery test system. CV tests were recorded with CHI1000 electrochemical workstation ranging from 0.01 to 3.0 V at a scan rate of $0.1 \text{ mV}\cdot\text{s}^{-1}$. Electrochemical impedance spectra (EIS) were carried out in the EnergyLab XM electrochemical workstation with an amplitude of 5 mV in the frequency range of 1×10^5 – 1×10^{-2} Hz.

3 Results and discussion

3.1 Morphological and structural characterization

The schematic diagram of the synthesis procedure of the carbon-coated $\text{Sb}/\text{Sb}_2\text{S}_3@/\text{Ti}_3\text{C}_2\text{T}_x$ composite is shown in Fig. 1. $\text{Sb}/\text{Sb}_2\text{S}_3$ nanoparticles were in situ formed on the surface of MXene, which can not only confine the growth of Sb and Sb_2S_3 , but also prevent their agglomeration. In turn, the uniformly distributed Sb-based particle can prevent MXene from collapsing and restacking. During the annealing process, the surface of $\text{Sb}/\text{Sb}_2\text{S}_3@/\text{Ti}_3\text{C}_2\text{T}_x$ would be covered by the ultra-thin carbon layer, which not only further relieves the volume expansion and increases the conductivity, but also protects MXene from oxidation, and refrains the direct contact between Sb-based material and electrolyte, thus decreasing the side reaction.

The morphology characterization of the as-prepared composites was measured by SEM. After etching from the massive Ti_3AlC_2 (Fig. S1), the few-layer MXene $\text{Ti}_3\text{C}_2\text{T}_x$

was obtained, as observed in Fig. 2a. SEM images of $\text{MX-Sb}/\text{Sb}_2\text{S}_3@/\text{C-1}$ in Fig. 2b, c show that a great number of $\text{Sb}/\text{Sb}_2\text{S}_3$ nanoparticles are uniformly distributed on the surface of lamellar $\text{Ti}_3\text{C}_2\text{T}_x$, which is covered by the ultra-thin carbon. The double confining effect of MXene and carbon can buffer the volume expansion of $\text{Sb}/\text{Sb}_2\text{S}_3$ more sufficiently and limit the particle growth simultaneously, which is due to the in situ fabrication process. According to the particle size distribution in Fig. S2, the average size of the nanoparticle is ~ 25 nm. TEM was further measured to survey the microstructure of $\text{MX-Sb}/\text{Sb}_2\text{S}_3@/\text{C-1}$ composite. As shown in Figs. 2d, e, S3, the MXene with transparent lamellar structure is loaded with evenly dispersed Sb-based nanoparticles, which is consistent with SEM results. The HRTEM image in Fig. 2f displays two kinds of lattice fringes with an interplanar spacing of 0.23 and 0.34 nm, respectively, responding to the (104) lattice plane of Sb and (111) lattice plane of Sb_2S_3 , which confirms the successful synthesis of the $\text{Sb}/\text{Sb}_2\text{S}_3$ heterostructure. Energy-dispersive spectroscopy (EDS) mapping of $\text{MX-Sb}/\text{Sb}_2\text{S}_3@/\text{C-1}$ in Fig. 2g reveals the uniform distribution of Ti, C, Sb and S, and it can be seen that the elements of Sb and S are mainly gathered at the position of nanoparticles. The ICP-OES was measured to investigate the content of metal elements, and the content of Sb and Ti is 19.45 wt% and 45.76 wt%, respectively, which are close to EDS results (Fig. S4). To investigate the effect of the amount of SbCl_3 on the morphology of the composite, $\text{MX-Sb}/\text{Sb}_2\text{S}_3@/\text{C-0.5}$ and 1.5 were also

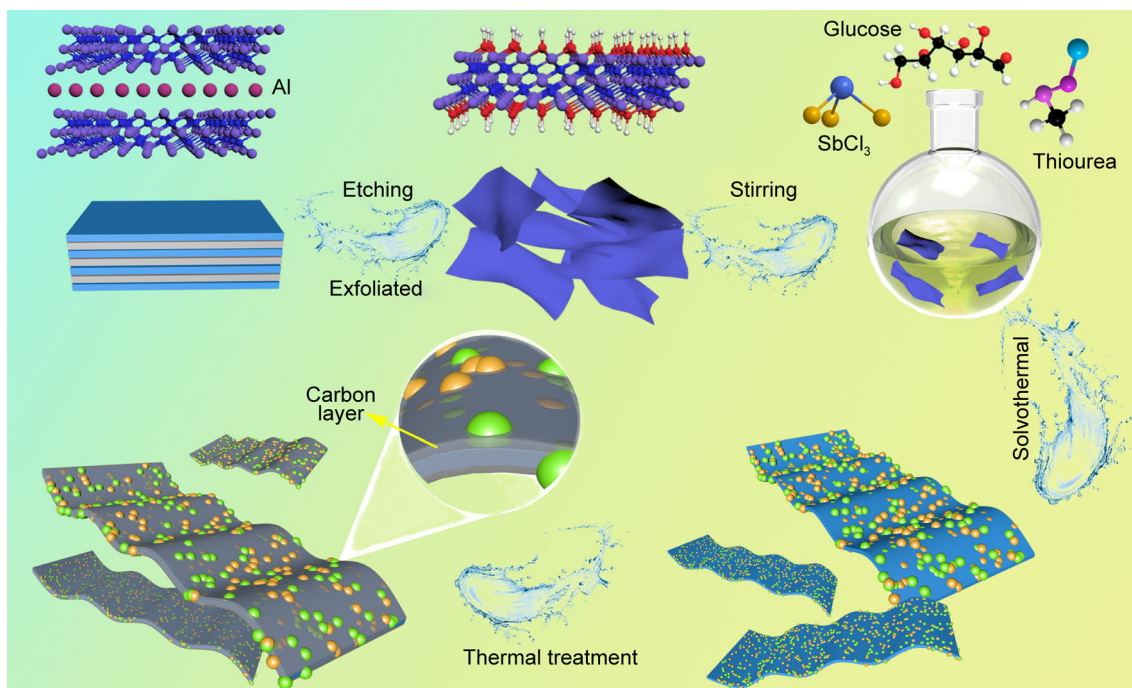


Fig. 1 Synthesis flowchart of carbon-coated $\text{Sb}/\text{Sb}_2\text{S}_3@/\text{Ti}_3\text{C}_2\text{T}_x$ composite

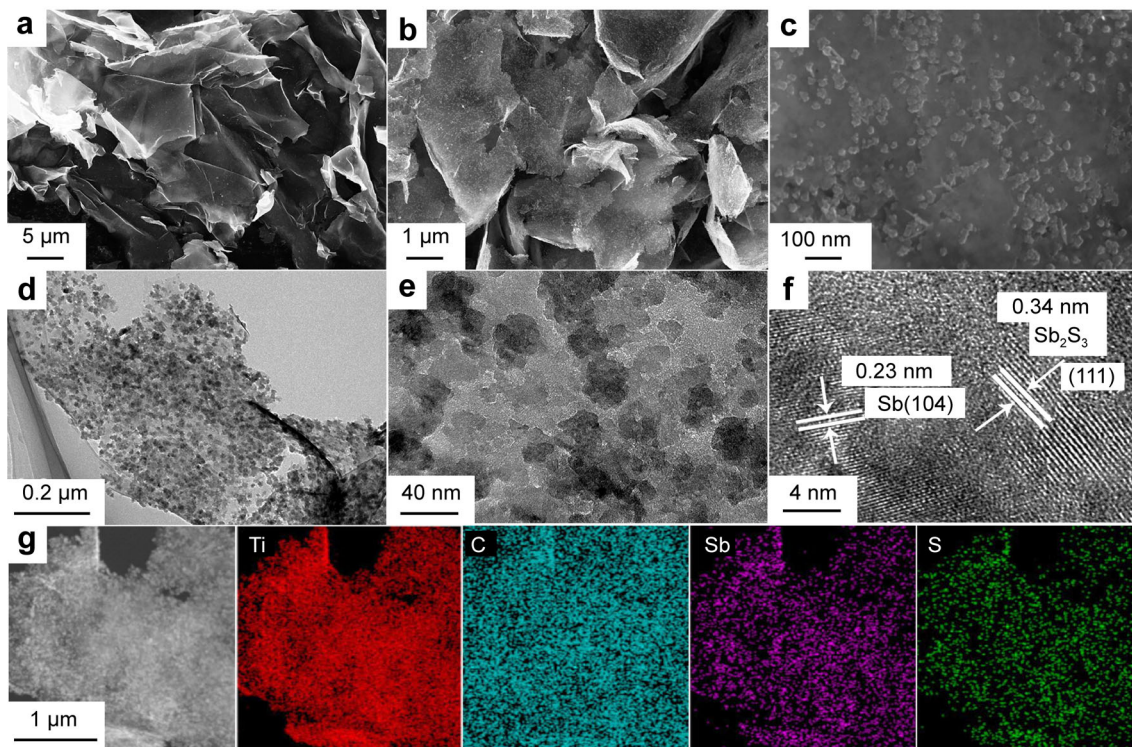


Fig. 2 SEM images of **a** Ti₃C₂T_x and **b, c** MX-Sb/Sb₂S₃@C-1; **d, e** TEM images, **f** HRTEM image and **g** EDS mappings of MX-Sb/Sb₂S₃@C-1

measured by SEM. As shown in Fig. S5, there is no obvious change in the overall morphology except that the nanoparticles on the MXene grew denser with the amount of SbCl₃ increased. In comparison, pure Sb₂S₃ shows serious aggregation and the particle sizes are larger than that of the composites (Fig. S6a). The commercial Sb shown in Fig. S6b is block.

XRD was adopted to analyze the crystal structure of the as-synthesized composites. As described in Fig. 3a, after etching with LiF, the peak of (008) and (105) in Ti₃AlC₂ (Fig. S7a) disappeared, indicating the formation of Ti₃C₂T_x. In addition, the peak of (002) in Ti₃C₂T_x shifts to a smaller angle ($\sim 6.69^\circ$) than that of Ti₃AlC₂, and the interlayer spacing is calculated to be 1.26 nm, which indicates that the lattice spacing increased significantly after etching. The three composites with different tin contents present similar XRD patterns, manifesting the same crystal structure. In these composites, except for the (002) peak of MXene, the diffraction peaks at 28.6°, 40°, 41.9° and 51.6° are responds to the (012), (104), (110) and (202) lattice planes of Sb (PDF No. 85-1322) [29]; and the peaks at 15.6°, 17.5°, 24.8° and 35.5° are accord with the (020), (120), (130) and (240) planes of Sb₂S₃ (PDF No. 42-1393) [30], demonstrating the successful formation of Sb/Sb₂S₃@MXene@C composite. No peak of carbon was observed due to the amorphous structure. The content ratio

of Sb to Sb₂S₃ is $\sim 3:1$ in MX-Sb/Sb₂S₃@C-1 according to the peak intensity. The Rietveld refined XRD profile of MX-Sb/Sb₂S₃@C-1 is shown in Fig. S8, and the content of Sb and Sb₂S₃ estimated from the Rietveld refinement is 64.27 wt% and 35.73 wt% (Table S1). Furthermore, the XRD patterns of pure Sb₂S₃ and commercial Sb were also measured, which matched the standard card very well (Fig. S7b, c).

To further explore the structure of the as-prepared composites, FTIR spectra were investigated. As displayed in Fig. 3b, the peaks that appeared at 1110 and 1460 cm⁻¹ in Ti₃C₂T_x are corresponding to O–H, and the peak at 1630 cm⁻¹ is the characteristic peak of C=O [31, 32]. Compared with pure Ti₃C₂T_x, the peak intensities in the composites of MX-Sb/Sb₂S₃@C-0.5/1/1.5 were reduced, which is related to the introduction of Sb-based material and carbon. The peak at 418 cm⁻¹ in MX-Sb/Sb₂S₃@C-0.5/1/1.5 is due to the presence of Sb and Sb₂S₃, and the peak at 660 cm⁻¹ is attributed to the bond of Sb–S. It is worth noting that the peaks at 565 and 710–840 cm⁻¹ exist only in the composite, which is related to the Ti–S and Ti–O–Sb bonds [33]. The FTIR test shows that the abundant oxygen-containing functional groups in Ti₃C₂T_x can bond with Sb/Sb₂S₃ nanoparticles via strong covalent bonds, which can improve the interface stability as well as accelerate the interfacial charge transfer. And the tight

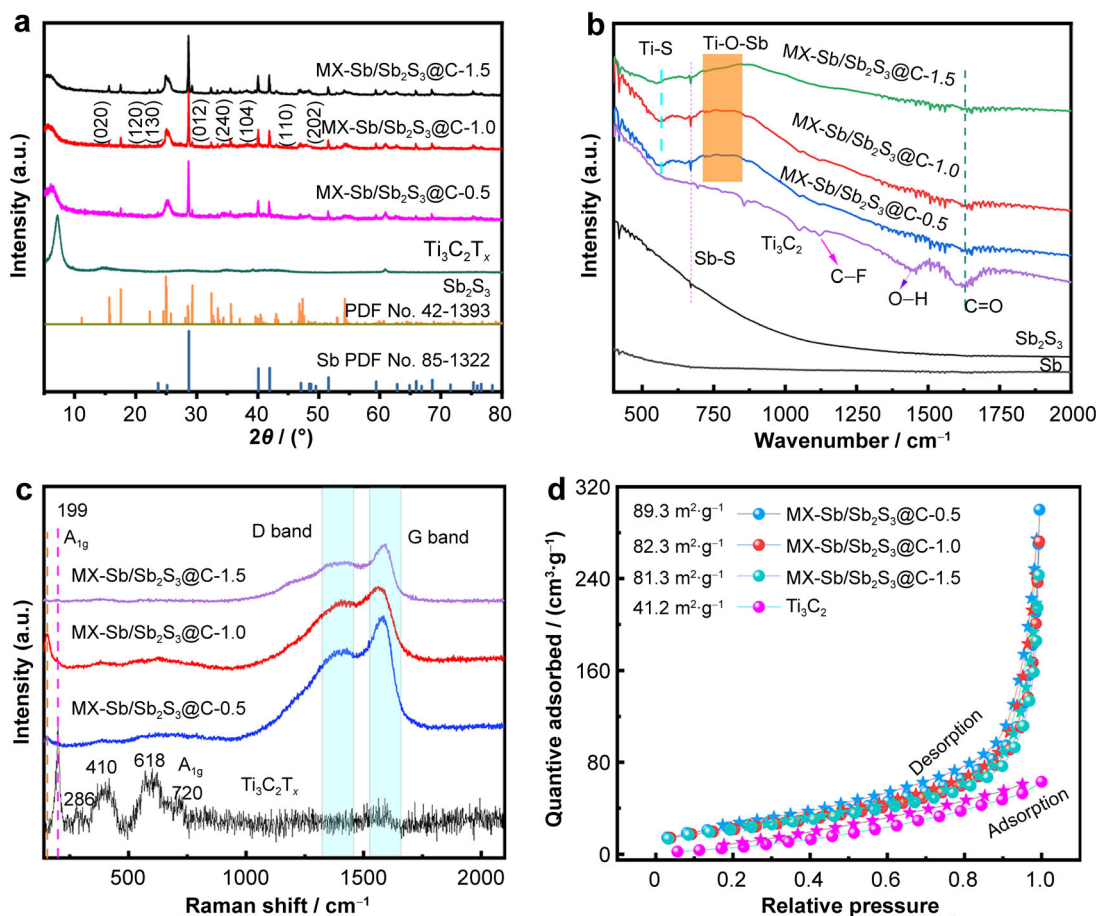


Fig. 3 a XRD patterns and b FTIR spectra of all prepared anodes. c Raman spectra and d N₂ adsorption/desorption curves of Ti₃C₂T_x and MX-Sb/Sb₂S₃@C-0.5/1.5

coupling of carbon and Ti₃C₂T_x can confine the nanoparticles adequately and prevent Ti₃C₂T_x from oxidation.

The Raman spectrum in Fig. 3c shows two kinds of characteristic peaks in Ti₃C₂T_x, the peaks at 199 and 720 cm⁻¹ rise from the A_{1g} vibrational mode, and the peaks at 286, 410 and 618 cm⁻¹ belong to the E_g vibrational mode [34]. In the MX-Sb/Sb₂S₃@C-0.5/1.5 composites, the peaks at 1380 and 1570 cm⁻¹ are ascribed to the D peak (disorder degree) and the G peak (graphitization degree) of carbon on the surface of the composites. In addition, the peak at 150 cm⁻¹ is attributed to Sb and Sb₂S₃, which is consistent with that of the pure Sb and Sb₂S₃ in Fig. S9. The specific surface areas of the electrode materials were tested from N₂ adsorption and desorption curves. As demonstrated in Fig. 3d, the specific surface area of pure Ti₃C₂T_x is 41.2 m²·g⁻¹, which is lower than that of MX-Sb/Sb₂S₃@C-0.5/1.5 with the surface areas of 89.3, 82.3 and 81.3 m²·g⁻¹, respectively. The higher surface area of the composite is related to the loading of Sb/Sb₂S₃ nanoparticles and the coated amorphous carbon.

However, with the increase in the content of SbCl₃, the surface area decreased slightly, which is related to the increased particle size as presented in the SEM images. Furthermore, the surface areas of pure Sb and Sb₂S₃ were measured to be 0.63 and 12.5 m²·g⁻¹ (Fig. S10). The pore size distribution of pure Ti₃C₂T_x is mainly concentrated in 1–10 nm, while for the composites, in addition to 1–10 nm, they also show peaks in the range of 10–20 nm (Fig. S11). Commonly, the large surface area and abundant pore distribution are beneficial for providing abundant reaction active sites and promoting electrolyte infiltration.

To explore the surface chemical state of the composite, XPS was carried out on MX-Sb/Sb₂S₃@C-1. As shown in the full spectrum in Fig. S12, the characteristic peaks of Ti, Sb, S and C can be observed. The high-resolution Sb 3d spectrum of MX-Sb/Sb₂S₃@C-1 can be split into two peaks (Fig. 4a) including Sb 3d_{5/2} (529.8, 530.6 eV) and Sb 3d_{3/2} (539.4, 540.1 eV). The peaks at 529.8 and 539.4 eV respond to metal Sb, and the peaks at 530.6 and 540.1 eV are ascribed to Sb³⁺ (Sb₂S₃) [18]. The O 1s

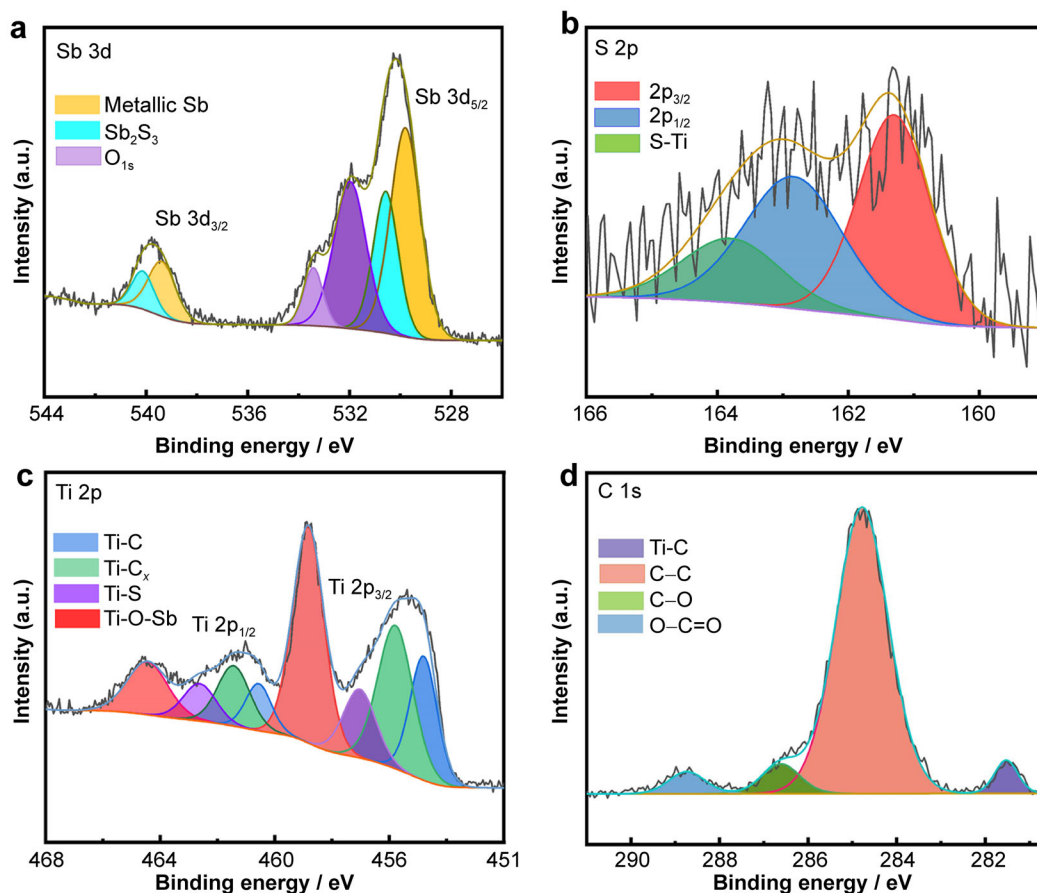


Fig. 4 XPS spectra of MX-Sb/Sb₂S₃@C-1: **a** Sb 3d, **b** S 2p, **c** Ti 2p and **d** C 1s

spectrum (531.9, 533.4 eV) demonstrates the existence of C–O–C and oxygen-containing functional groups [35]. The S 2p spectrum in Fig. 4b can be divided into three peaks. The peaks of S 2p_{3/2} (161.3 eV) and S 2p_{1/2} (162.8 eV) are responding to S²⁻ in Sb₂S₃ [36]. The peak at 163.8 eV is due to the Ti–S bond between Ti₃C₂T_x and Sb₂S₃, which conforms to the FTIR results (Fig. 3b). The Ti 2p spectrum (Fig. 4c) includes (454.8, 460.6 eV), Ti–C_x (non-stoichiometric defects, $x < 1$, 455.8, 461.4 eV), Ti–S (457.1, 462.6 eV) and Ti–O–Sb (458.8, 464.5 eV) bonds [37]. In addition, the C 1s spectrum in Fig. 4d can be divided into four types. The peaks at 284.8 and 288.8 eV respond to C–C and O–C=O bonds [38]. The peaks at 286.6 and 281.5 eV are ascribed to C–O (C–O–Sb) and Ti–C bonds. XPS results confirm that the Sb/Sb₂S₃ nanoparticles can combine with the conductive substrate (MXene and carbon) via strong covalent bonds, which can not only confine the Sb/Sb₂S₃ nanoparticles to reduce the particles aggregation and relieve the volume expansion, and then improve the stability and integrity of the composite, but also enhance charge mobility and boost the rate performance.

3.2 Electrochemical characterization

The sodium-ion storage performances of the composites were examined using half batteries. CV curves of MX-Sb/Sb₂S₃@C-1 for the first 3 cycles under 0.1 mV·s⁻¹ between 0.01 and 2.0 V are shown in Fig. 5a. There is an obvious difference between the curves of the first and the following cycles due to the activated process at the beginning. There are three reduction peaks at 1.2, 0.78 and 0.2 V for the first cycle. The peak at 1.2–0.78 V is ascribed to the conversion reaction of Sb₂S₃ as shown in Eq. (1) and the formation of the solid electrolyte films (SEI) on the surfaces of the electrode [39]. The peak below 0.2 V corresponds to the alloying reaction between Sb and Na⁺ (Reactions (2, 3)) as well as the insertion of Na⁺ into Ti₃C₂T_x and carbon. Accordingly, the oxidation peaks located at 0.85 and 1.61 V reflect the dealloying reaction and conversion reaction. The small oxidation peak around 2.1 V is derived from the multiple reactions of the interface between Sb-based nanoparticles and Ti₃C₂T_x (combined with a covalent bond like Ti–O–Sb) [28]. The curves of the second and third cycles overlapped quite well, indicating

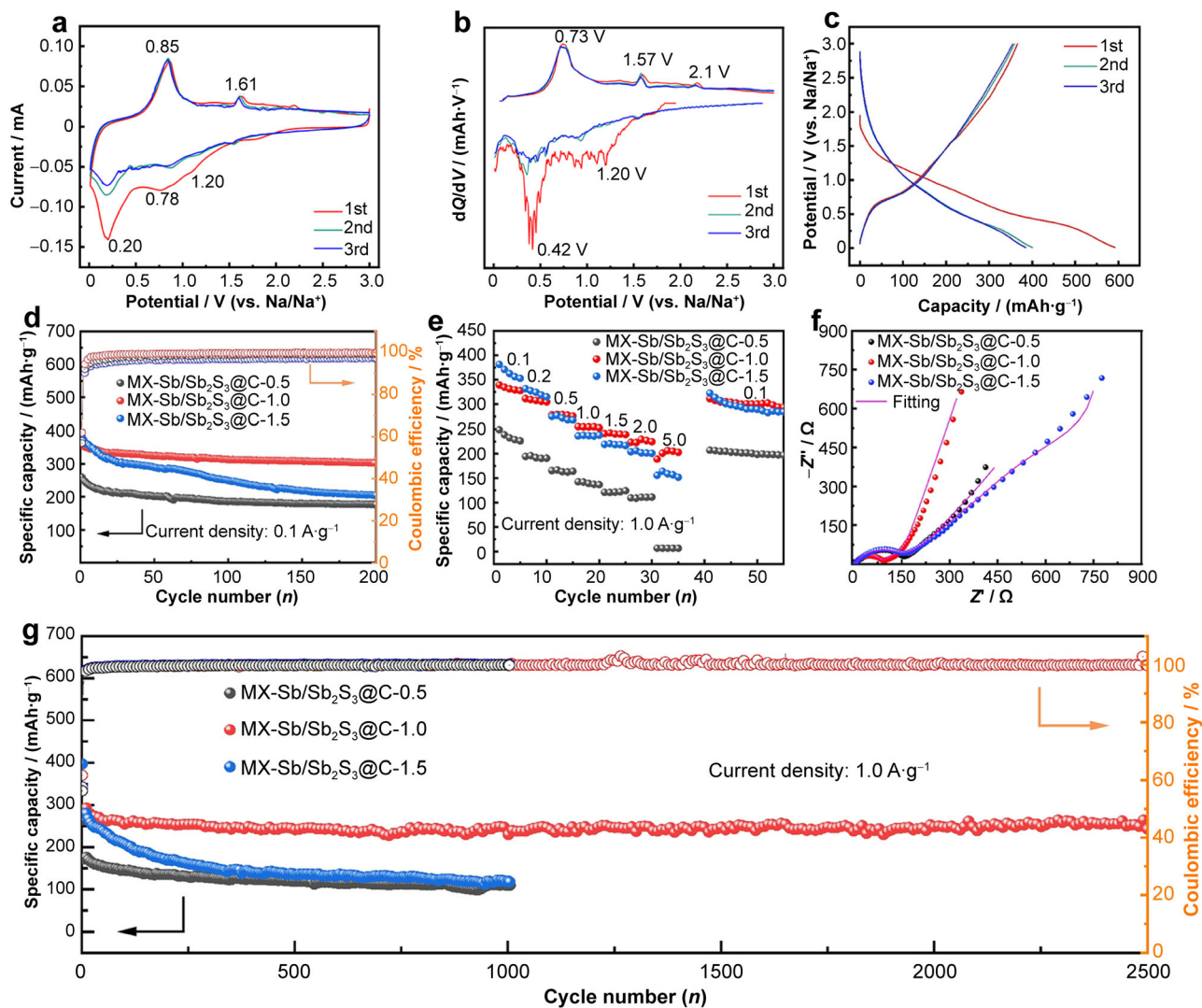
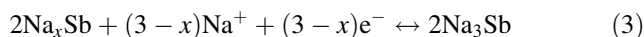
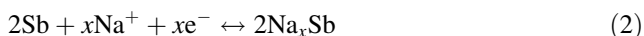
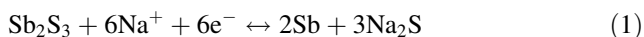


Fig. 5 **a, b** CV and differential capacitance curves of MX-Sb/Sb₂S₃@C-1 at 0.1 mV·s⁻¹; **c** charge/discharge curves of MX-Sb/Sb₂S₃@C-1 at 0.1 A·g⁻¹; electrochemical property of MX-Sb/Sb₂S₃@C-0.5/1/1.5; **d** cycle performance at 0.1 A·g⁻¹; **e** rate property; **f** EIS spectra; **g** cycle property at 1.0 A·g⁻¹

the excellent reversibility and stability of the electrode. This phenomenon also occurred in the differential capacitance curves of MX-Sb/Sb₂S₃@C-1 in Fig. 5b. The CV test and differential capacitance curve analysis were also carried out on pure Sb₂S₃ and commercial Sb as shown in Fig. S13. The shape of the curve of Sb₂S₃ is similar to that of MX-Sb/Sb₂S₃@C-1, including the conversion reaction at around 1.22 V and the following alloying reaction. For pure Sb, there is only the peak responding to the alloying reaction at 0.48 V. However, both pure Sb₂S₃ and pure Sb display inferior reversibility during the following cycles, which decreases the utilization of the electrodes.



The galvanostatic charge–discharge tests were executed on the electrode materials. Figure 5c reveals the charge–discharge curves of MX-Sb/Sb₂S₃@C-1 under the current density of 0.1 A·g⁻¹. The initial discharge/charge capacities were 592/366 mAh·g⁻¹ with an initial coulomb efficiency (ICE) of 62%. The high capacity profited from the unique structure, which provides efficient electronic transmission paths and promotes the ion diffusion. The irreversible capacity for the first cycle is ascribed to the side reaction between the electrode and electrolyte. After that, the capacity was stabilized at 355 mAh·g⁻¹ with CE of 93% (the 3rd cycle). To investigate the effect of the content of tin on the sodium-ion storage, the cycle performances of MX-

Sb/Sb₂S₃@C-0.5/1/1.5 composites under 0.1 A·g⁻¹ were tested as exhibited in Fig. 5d. It can be seen that MX-Sb/Sb₂S₃@C-1.5 with the maximum loading of Sb/Sb₂S₃ shows the highest capacity of 382 mAh·g⁻¹ for the first cycle among the three composites, but it decayed rapidly to only 204 mAh·g⁻¹ after 200 cycles. Similarly, without the support of MXene and carbon substrate, the capacities of pure Sb and Sb₂S₃ descend like a cliff after around 20 cycles although they had high initial capacities. And pure Ti₃C₂T_x only delivers a capacity of 24 mAh·g⁻¹ (Fig. S14a). By contrast, the other two composites demonstrate remarkable cycle stability without capacity decay after 200 cycles (177 mAh·g⁻¹ for MX-Sb/Sb₂S₃@C-0.5 and 302 mAh·g⁻¹ for MX-Sb/Sb₂S₃@C-1) benefitting from the double confine protection of MXene and carbon as well as the uniform distribution of nanoparticles, which can fully relieve the volume expansion of Sb-based materials and prevent aggregation. To further survey the long cycle performances, the electrodes were measured under 1 A·g⁻¹. As displayed in Fig. 5g, MX-Sb/Sb₂S₃@C-1 composite displayed fairly outstanding stability with a reversible capacity of 250 mAh·g⁻¹ even after 2500 cycles with a low attenuation rate of only 0.0228 mAh·g⁻¹ for each cycle. It is much higher than that of MX-Sb/Sb₂S₃@C-0.5 with the residual capacity of 110 mAh·g⁻¹ and MX-Sb/Sb₂S₃@C-1.5 of 120 mAh·g⁻¹ after 1000 cycles. All the composites deliver a much higher capacity than pure Sb, Sb₂S₃ and MXene under large currents for long cycles as shown in Fig. S15. It can be concluded that not only the structure design but also the loading content affect the storage performance of the materials significantly.

Figure 5e displays the rate performances of MX-Sb/Sb₂S₃@C-0.5/1/1.5 from 0.1 to 5 A·g⁻¹. MX-Sb/Sb₂S₃@C-1 delivers capacities of 332.4, 307.8, 278.2, 253.7, 240.1 and 225 mAh·g⁻¹ under 0.1, 0.2, 0.5, 1.0, 1.5 and 2 A·g⁻¹. As the current density increased to 5 A·g⁻¹, it can still maintain the high capacity of 200.5 mAh·g⁻¹. As the current density recovers to 0.1 A·g⁻¹, the capacity can still return to 306.5 mAh·g⁻¹. MX-Sb/Sb₂S₃@C-1 presents an obvious advantage compared with MX-Sb/Sb₂S₃@C-0.5 and MX-Sb/Sb₂S₃@C-1.5, and much better than pure Sb, Sb₂S₃ and Ti₃C₂T_x (Fig. S14b). It is also worth noting that the sodium storage property of MX-Sb/Sb₂S₃@C-1 is better than most reported Sb-based anode materials (Table S2). To further discuss the structure stability of MX-Sb/Sb₂S₃@C-1, SEM was carried out after 200 cycles. As displayed in Fig. S16, the surface of the electrode was still quite smooth after the cycle, and the nanoparticles were still firmly anchored on the surface of lamellar Ti₃C₂T_x, which is due to the strong interaction force between the Sb-based material, MXene and carbon by the covalence bond derive from the in situ formation process.

The electrochemical impedance spectroscopies of MX-Sb/Sb₂S₃@C-0.5/1/1.5 are shown in Fig. 5f, which were tested with a frequency range of 1×10⁵–1×10⁻² Hz at a perturbation AC potential of 5 mV. All the Nyquist curves contain a half circle in high-frequency region and a slash in low-frequency region. The slope of the slash represents the Na⁺ diffusion coefficient; the larger the slope, the faster the diffusion. The half circle reflects the electrolyte transfer impedance (*R_s*) and charge transfer impedance (*R_{ct}*). Table S3 shows the impedance fitting parameters of all the samples. Compared with pure Sb, Sb₂S₃ and Ti₃C₂T_x (Fig. S14c), all the composites show obvious decreased impedance, which confirms that the interfacial chemical bonding and heterostructure design can improve ion diffusion kinetics and accelerate the charge transfer.

Furthermore, EIS of MX-Sb/Sb₂S₃@C-1 electrode was measured at various states of charge (Fig. 6a). *R_{ct}* decreased from 527 Ω (before discharging) to 233.4 Ω (discharged to 0.7 V), and it kept decreasing during the following discharging process on the whole with occasional rising, which may be due to that the formed SEI layer blocks the charge transfer (Table S4). During the charging process, the *R_{ct}* decreased obviously and it turned to 80.62 Ω when charged to 3.0 V. The same tendency was also observed in the value of *R_s*. It can be seen that MX-Sb/Sb₂S₃@C-1 was activated gradually during the first lap, which helps reduce the polarization.

CV curves of MX-Sb/Sb₂S₃@C-1 under different scan rates of 0.1, 0.2, 0.6, 0.8 and 1.0 mV·s⁻¹ were tested to reveal the dynamic characteristic as shown in Fig. 6b. With the increase in the scan rate, the position of the peak shifts slightly, which is due to the polarization of the electrode. The peak current (*i*) and scan rate (*v*) conform to the exponential relation as described in Eq. (4),

$$i = av^b \quad (4)$$

where *a* and *b* are constants. The value of *b* can be calculated according to the functional relationship between *lgi* and *lgv* as shown in the inset in Fig. 6b. Commonly, the value of *b* is between 0.5 and 1.0. When the value of *b* approaches 0.5, the electrochemical behavior is mainly controlled by diffusion processes. When the value is close to 1.0, the surface capacitance process dominates. The values of *b* calculated from the oxidation peak and reduction peak are 0.85 and 0.9, manifesting that the electrochemical behavior of MX-Sb/Sb₂S₃@C-1 was controlled by surface pseudocapacitance. The capacitive contribution can be further quantified according to Eqs. (5, 6),

$$lgi = blgv + lga \quad (5)$$

$$i(V) = i_{cap} + i_{diff} = k_1v + k_2v^{1/2} \quad (6)$$

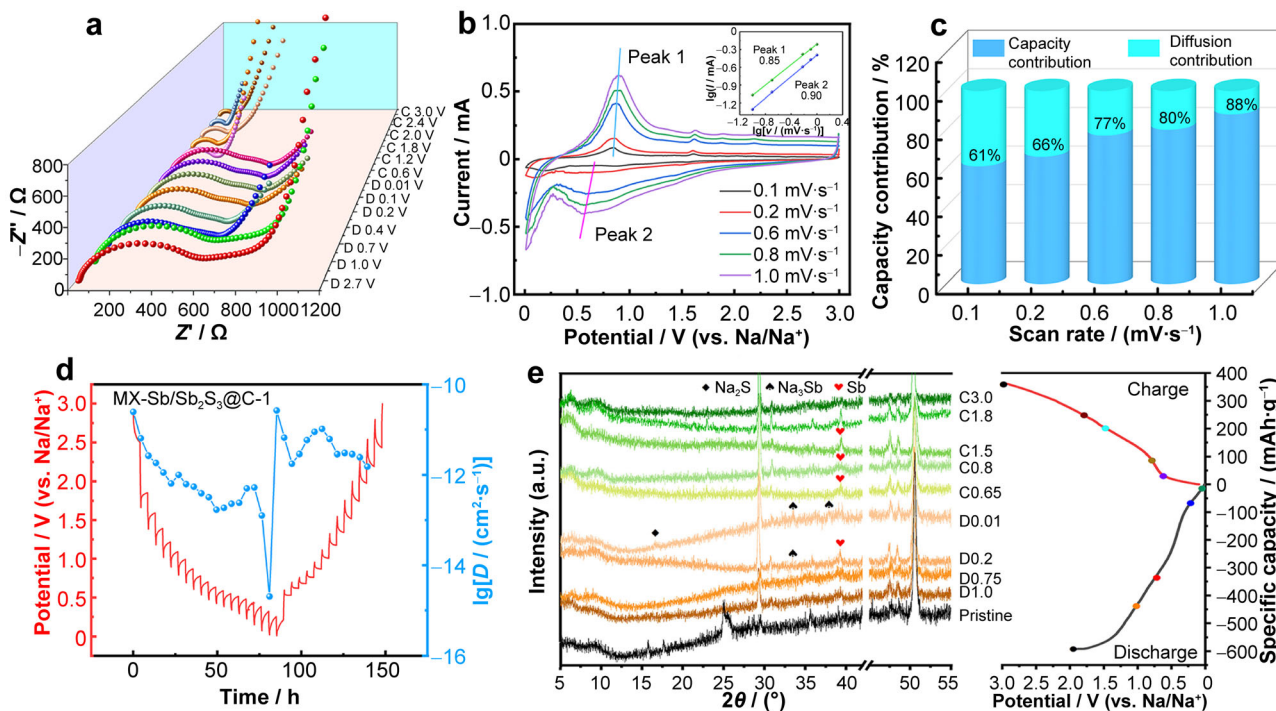


Fig. 6 **a** Ex situ electrochemical impedance spectroscopy; **b** CV curves at different scan rates and (inset) $\lg i$ versus $\lg v$ plots; **c** capacity contribution ratio; **d** GITT curves; **e** ex situ XRD patterns of MX-Sb/Sb₂S₃@C-1

where v is the scan rate, k_1 and k_2 are constants, i_{cap} is the current required to charge the double layer at the electrolyte interface and i_{diff} is the current related to the slow diffusion-controlled process. The value of $k_1 v$ reflects the contribution of pseudocapacitance control, and $k_2 v^{1/2}$ represents the contribution of diffusion control. Figure 6c presents the capacitance contribution ratio of MX-Sb/Sb₂S₃@C-1 under different scan rates, showing that the capacitance contribution increased with the increase in the scan rate. The contribution ratio of capacitance raised to 88% under the scan rate of 1 mV·s⁻¹, manifesting that the capacitance behavior plays an important role in sodium storage, especially under a large current density.

Moreover, galvanostatic intermittent titration technique (GITT) is a common method to evaluate the Na⁺ diffusion coefficient, which can visually reflect the diffusion kinetics of Na⁺ in the anode. According to Eq. (7),

$$D = \frac{4}{\pi\tau} \left(\frac{m_B V_M}{M_B S} \right)^2 \left(\frac{\Delta E_s}{\Delta E_\tau} \right)^2 \quad (7)$$

where τ means the time of the constant current applied (30 min); m_B , V_M , M_B and S represent the mass of active substance, molar volume, molar mass and area, respectively; ΔE_s and ΔE_τ are the change in equilibrium potential after a current pulse and the transient potential changes throughout the pulse, respectively. Figure 6d displays GITT curve of MX-Sb/Sb₂S₃@C-1. It can be discovered that during the discharging/charging process, the diffusion

coefficient shows a downward trend of fluctuation. While during the transient period from the discharging process to the charging process, the diffusion coefficient increased suddenly. Usually, if the diffusion coefficient during the discharging process is smaller than that in the charging procedure, it means that the process of sodium removal is easier than the process of sodium insertion. The average value of $\lg D$ of MX-Sb/Sb₂S₃@C-1 is calculated to be -11 . In comparison, the MX-Sb/Sb₂S₃@C-1 shows a higher diffusion coefficient than that of pure Sb and Sb₂S₃ (Fig. S17), which may due to the small size of the particles and the effect of MXene and carbon in the composite.

To in-depth understand the sodium storage mechanism of MX-Sb/Sb₂S₃@C-1, the ex situ XRD test was executed. As shown in Fig. 6e, all the characteristic peaks in MX-Sb/Sb₂S₃@C-1 can be observed under the open-circuit potential (including Sb, Sb₂S₃ and MXene). When the electrode was discharged to 1 V, the peak intensity of the Sb₂S₃ decreased greatly, indicating the conversion reaction procedure. When the anode was discharged to 0.2 V, a new peak at 33.5° appeared, which is ascribed to the (110) lattice plane of Na₃Sb (PDF No. 740-1162), reflecting the alloying reaction process between Sb and Na⁺. And when the electrode was discharged to 0.01 V, the peak of Sb disappeared, and the peak intensity of Na₃Sb increased significantly. In the meantime, the peak at 16.7° still exists, which is Na₂S (PDF No. 47-0178) derived from the conversion reaction of Sb₂S₃ and Na⁺. During the charging state at 0.65 V, the peak of Na₃Sb disappeared and

the peak of Sb reappeared. This phenomenon confirms the reversible alloying reaction process. When the cell was charged to 3.0 V, the peak intensity of Sb decreased, meaning the partial conversion from Sb to Sb₂S₃. No characteristic peak of Sb₂S₃ was detected after charging, which may be related to the weak crystallinity of Sb₂S₃. Based on the above analysis, the sodium storage mechanism of MX-Sb/Sb₂S₃@C-1 includes the totally alloying reaction of Sb and the partially reversible conversional reaction of Sb₂S₃.

To fully explore the energy storage potential of the MX-Sb/Sb₂S₃@C-1, the lithium-ion storage performance was also investigated. The CV curves were measured from 0.01 to 3 V in LIBs. As observed in Fig. S18a, there are three obvious reduction peaks at 1.7, 1.36 and 0.64 V for the first cycle, responding to the conversion reaction of Sb₂S₃, the alloying reaction of Sb and the formation of SEI film [18]. The peak below 0.3 V is related to the insertion of Li⁺ in Ti₃C₂T_x and carbon. The oxidation peaks appeared at 1.13, 1.98 and 2.35 V, which presents the dealloying reaction (2Li₃Sb → 2Sb + 6Li⁺ + 6e⁻) and the formation of Sb₂S₃ (2Sb + 3Li₂S → Sb₂S₃ + 6Li⁺ + 6e⁻). The coincidence of curves for the following cycles manifests the perfect reversibility of the anode. The constant current charge and discharge curve of MX-Sb/Sb₂S₃@C-1 at 0.1 A·g⁻¹ are shown in Fig. S18b. The initial discharge/charge capacities are as high as 735/479.5 mAh·g⁻¹. It can still maintain 479.5 mAh·g⁻¹ after 100 cycles at 0.1 A·g⁻¹ (Fig. S18c) and 231 mAh·g⁻¹ after 300 cycles at 1.0 A·g⁻¹ (Fig. S18e). MX-Sb/Sb₂S₃@C-1 also shows excellent rate performance with the capacity of 464.9, 430.4, 395.7, 364.5 and 34.3 mAh·g⁻¹ under 0.1, 0.2, 0.5, 1.0 and 1.5 A·g⁻¹, respectively. When the current density returns to 0.1 A·g⁻¹ after the large current charge/discharge, the electrode can recover to 452.6 mAh·g⁻¹ (Fig. S18d). The outstanding lithium storage property of MX-Sb/Sb₂S₃@C-1 can be ascribed to the synergistic effect of MXene/carbon double-matrix and the heterogeneous Sb/Sb₂S₃ nanostructure design. The in situ preparation method enables the firm anchoring of Sb/Sb₂S₃ nanoparticles on the surface of MXene covered by carbon, and it can not only confine the overgrowth of Sb-based material, but also adequately buffer the volume expansion and improve the conductivity and then effectively improve the stability and kinetic reaction rate of the Sb-based materials.

4 Conclusion

The Sb/Sb₂S₃@Ti₃C₂T_x@C double-confined nanoheterostructure composites have been successfully fabricated by a facial one-step solvothermal method followed by low-temperature heat treatment. Ultra-small Sb and Sb₂S₃ nanoparticles are uniformly distributed on the surface of Ti₃C₂T_x nanosheets

covered by ultra-thin carbon layers. The unique double-confined structure design can not only better accommodate the volume expansion and facilitate the rapid transport of ions and electrons, but also preserve the structural integrity due to the strong interfacial coupling (Ti–S, Ti–O–Sb). Moreover, the heterogeneous interface between Sb and Sb₂S₃ can further promote charge transfer. Benefits from the unique structure, MX-Sb/Sb₂S₃@C-1 with the optimal tin content exhibited the ultra-stable cycle performance with a reversible capacity of 250 mAh·g⁻¹ at 1.0 A·g⁻¹ after 2500 cycles and comparable rate property with 200.5 mAh·g⁻¹ under 5 A·g⁻¹ in SIBs. The composites also exhibited excellent lithium storage performances. The ex situ XRD revealed the storage mechanism of MX-Sb/Sb₂S₃@C-1 including the alloying reaction and conversional procedure. The pseudocapacitance test proved that the capacitive behavior is dominant in MX-Sb/Sb₂S₃@C-1 (1 mV·s⁻¹, 88%). This work highlights the necessity of architectural engineering in realizing advanced anode materials.

Acknowledgements This study was financially supported by the National Natural Science Foundation of China (Nos. 52071073, 52177208, 52171202 and 51971055), Hebei Province “333 talent project” (No. C20221012), the Natural Science Foundation of Hebei Province (No. E2020501004), the Fundamental Research Funds for the Central Universities (No. N2123032) and the Science and Technology Project of Hebei Education Department (No. BJK2023005).

Declarations

Conflict of interests The authors declare that they have no conflict of interest.

References

- [1] Delmas C. Sodium and sodium-ion batteries: 50 years of research. *Adv Energy Mater.* 2018;8(17):1703137. <https://doi.org/10.1002/aenm.201703137>.
- [2] Nayak PK, Yang L, Brehm W, Adelhelm P. From lithium-ion to sodium-ion batteries: advantages, challenges, and surprises. *Angew Chem Int Ed Engl.* 2018;57(1):102. <https://doi.org/10.1002/anie.201703772>.
- [3] Han JH, He J, Zou QY, Zhang J, Yang Z, Zhao ZW, Chen HX, Yue HJ, Wang DW, Lin HC, Liu HD, Zhong GM, Peng ZQ. High-capacity potassium ion storage mechanisms in a soft carbon revealed by solid-state NMR spectroscopy. *Rare Met.* 2022; 41(11):3752. <https://doi.org/10.1007/s12598-022-02063-5>.
- [4] Song K, Liu C, Mi L, Chou S, Chen W, Shen C. Recent progress on the alloy-based anode for sodium-ion batteries and potassium-ion batteries. *Small.* 2021;17(9):1903194. <https://doi.org/10.1002/sml.201903194>.
- [5] Zhang W, Zhang F, Ming F, Alshareef HN. Sodium-ion battery anodes: status and future trends. *EnergyChem.* 2019;1(2): 100012. <https://doi.org/10.1016/j.enchem.2019.100012>.
- [6] Fu Y, Wei Q, Zhang G, Sun S. Advanced phosphorus-based materials for lithium/sodium-ion batteries: recent developments and future perspectives. *Adv Energy Mater.* 2018;8(13): 1703058. <https://doi.org/10.1002/aenm.201702849>.
- [7] Fu T, Li PC, He HC, Ding SS, Cai Y, Zhang M. Electrospinning with sulfur powder to prepare CNF@G-Fe₉S₁₀ nanofibers with controllable particles distribution for stable potassium-ion



- storage. *Rare Met.* 2022;42(1):111. <https://doi.org/10.1007/s12598-022-02103-0>.
- [8] Luo W, Ren J, Feng W, Chen X, Yan Y, Zahir N. Engineering nanostructured antimony-based anode materials for sodium ion batteries. *Coatings.* 2021;11(10):1233. <https://doi.org/10.3390/coatings11101233>.
- [9] Chong S, Qiao S, Wei X, Li T, Yuan L, Dong S, Huang W. Sb₂S₃-based conversion-alloying dual mechanism anode for potassium-ion batteries. *iScience.* 2021;24(12):103494. <https://doi.org/10.1016/j.isci.2021.103494>.
- [10] Yao S, Cui J, Deng Y, Chong WG, Wu J, Ihsan-Ul-Haq M, Mai YW, Kim JK. Ultrathin Sb₂S₃ nanosheet anodes for exceptional pseudocapacitive contribution to multi-battery charge storage. *Energy Storage Mater.* 2019;20:36. <https://doi.org/10.1016/j.ensm.2018.11.005>.
- [11] Li D, Zhao S, Li J, Yuan Z, Cao J, Fu X, Zhang Y, Wang L, Han W. Ultrafine Sb₂S₃@carbon-nanofibers for fast and stable sodium storage. *Electrochim Acta.* 2022;411(10):140067. <https://doi.org/10.1016/j.electacta.2022.140067>.
- [12] Xia J, Zhang X, Yang Y, Wang X, Yao J. Electrospinning fabrication of flexible, foldable, and twistable Sb₂S₃/TiO₂/C nanofiber anode for lithium ion batteries. *Chem Eng J.* 2021; 413(1):127400. <https://doi.org/10.1016/j.cej.2020.127400>.
- [13] Zhang Z, Zhao J, Xu M, Wang H, Gong Y, Xu J. Facile synthesis of Sb₂S₃/MoS₂ heterostructure as anode material for sodium-ion batteries. *Nanotechnology.* 2018;29(33):335401. <https://doi.org/10.1088/1361-6528/aac645>.
- [14] Jia R, Li L, Shen G, Chen D. Hierarchical Sb₂S₃/SnS₂/C heterostructure with improved performance for sodium-ion batteries. *Sci China Mater.* 2022;65(6):1443. <https://doi.org/10.1007/s40843-021-1931-0>.
- [15] Li X, Liang H, Liu X, Sun R, Qin Z, Fan H, Zhang Y. Ion-exchange strategy of CoS₂/Sb₂S₃ hetero-structured nanocrystals encapsulated into 3D interpenetrating dual-carbon framework for high-performance N^{a+}/K⁺ batteries. *Chem Eng J.* 2021;425(1):130657. <https://doi.org/10.1016/j.cej.2021.130657>.
- [16] Ke G, Wu X, Chen H, Li W, Fan S, Mi H, Li Y, Zhang Q, He C, Ren X. Unveiling the reaction mechanism of an Sb₂S₃-Co₉S₈/NC anode for high-performance lithium-ion batteries. *Nanoscale.* 2021;13(47):20041. <https://doi.org/10.1039/d1nr06069d>.
- [17] Dong S, Li C, Ge X, Li Z, Miao X, Yin L. ZnS-Sb₂S₃@C core-double shell polyhedron structure derived from metal-organic framework as anodes for high performance sodium ion batteries. *ACS Nano.* 2017;11(6):6474. <https://doi.org/10.1021/acsnano.7b03321>.
- [18] Li C, Song H, Mao C, Peng H, Li G. A novel MoS₂ nanosheets-decorated Sb@Sb₂S₃@C tubular composites as anode material for high performance lithium ion battery. *J Alloys Compd.* 2019;786(25):169. <https://doi.org/10.1016/j.jallcom.2019.01.315>.
- [19] Wu Y, Zheng J, Tong Y, Liu X, Sun Y, Niu L, Li H. Carbon hollow tube-confined Sb/Sb₂S₃ nanorod fragments as highly stable anodes for potassium-ion batteries. *ACS Appl Mater Interfaces.* 2021;13(43):51066. <https://doi.org/10.1021/acsmi.1c16267>.
- [20] Xu X, Zhang Y, Sun H, Zhou J, Yang F, Li H, Chen H, Chen Y, Liu Z, Qiu Z, Wang D, Ma L, Wang J, Zeng Q, Peng Z. Progress and perspective: MXene and MXene-based nanomaterials for high-performance energy storage devices. *Adv Electron Mater.* 2021;7(7):2000967. <https://doi.org/10.1002/aelm.202000967>.
- [21] VahidMohammadi A, Mojtavani M, Caffrey NM, Wanunu M, Beidaghi M. Assembling 2D MXenes into highly stable pseudocapacitive electrodes with high power and energy densities. *Adv Mater.* 2019;31(8):1806931. <https://doi.org/10.1002/adma.201806931>.
- [22] Zhang H, Xiong D, Xu C, Xie Y, Zeng L, Feng Z, He M, Liu Q. VSe₂/MXene composite with hierarchical three-dimensional structure encapsulated in dopamine as an anode for potassium-ion batteries. *Electrochim Acta.* 2022;421(20):140487. <https://doi.org/10.1016/j.electacta.2022.140487>.
- [23] Li P, Zang R, Wu Y, Liu S, Wang S, Liu P, Li P. A quasi-3D Sb₂S₃/reduced graphene oxide/MXene (Ti₃C₂T_x) hybrid for high-rate and durable sodium-ion batteries. *Nanoscale.* 2022; 14(14):5529. <https://doi.org/10.1039/d2nr00655nc>.
- [24] Wang T, Shen D, Liu H, Chen H, Liu Q, Lu B. A Sb₂S₃ nanoflower/MXene composite as an anode for potassium-ion batteries. *ACS Appl Mater Interfaces.* 2020;12(52):57907. <https://doi.org/10.1021/acsmi.0c18285>.
- [25] Zhu M, Deng X, Feng Z, He M, Feng Y, Xiong D. Graphite nano-modified SnO₂-Ti₂C MXene as anode material for high-performance lithium-ion batteries. *J Alloys Compd.* 2021; 886(15):161139. <https://doi.org/10.1016/j.jallcom.2021.161139>.
- [26] Ren M, Cao D, Jiang W, Su K, Pan L, Jiang Y, Yan S, Qiu T, Yang M, Yang J, Zhang C. Hierarchical composite of Sb₂S₃ decorated on highly crumpled Ti₃C₂T_x nanosheets for enhanced sodium storage properties. *Electrochim Acta.* 2021;373(20): 137835. <https://doi.org/10.1016/j.electacta.2021.137835>.
- [27] Zhao J, Li CL, Chen G, Ji F, Shen YY, Peng J, Wang WH. Rational design of Sn₄P₃/Ti₃C₂T_x composite anode with enhanced performance for potassium-ion battery. *Rare Met.* 2022;41(7):2259. <https://doi.org/10.1007/s12598-021-01934-7>.
- [28] Wang H, Song X, Lv M, Jin S, Xu J, Kong X, Li X, Liu Z, Chang X, Sun W, Zheng J, Li X. Interfacial covalent bonding endowing Ti₃C₂-Sb₂S₃ composites high sodium storage performance. *Small.* 2022;18(3):2104293. <https://doi.org/10.1002/sml.202104293>.
- [29] Jing WT, Zhang Y, Gu Y, Zhu YF, Yang CC, Jiang Q. N-doped carbon nanonecklaces with encapsulated Sb as a sodium-ion battery anode. *Matter.* 2019;1(3):720. <https://doi.org/10.1016/j.matt.2019.03.010>.
- [30] Xie J, Liu L, Xia J, Zhang Y, Li M, Ouyang Y, Nie S, Wang X. Template-free synthesis of Sb₂S₃ hollow microspheres as anode materials for lithium-ion and sodium-ion batteries. *Nanomicro Lett.* 2018;10(1):12. <https://doi.org/10.1007/s40820-017-0165-1>.
- [31] Zhao N, Zhang F, Zhan F, Yi D, Yang Y, Cui W, Wang X. Fe³⁺-stabilized Ti₃C₂T_x MXene enables ultrastable Li-ion storage at low temperature. *J Mater Sci Technol.* 2021;67(20):156. <https://doi.org/10.1016/j.jmst.2020.06.037>.
- [32] Shen L, Zhao W, Wang K, Xu J. GO-Ti(3)C(2) two-dimensional heterojunction nanomaterial for anticorrosion enhancement of epoxy zinc-rich coatings. *J Hazard Mater.* 2021;417(5):126048. <https://doi.org/10.1016/j.jhazmat.2021.126048>.
- [33] Zhao R, Di H, Wang C, Hui X, Zhao D, Wang R, Zhang L, Yin L. Encapsulating ultrafine Sb nanoparticles in Na⁺ pre-intercalated 3D porous Ti₃C₂T_x MXene nanostructures for enhanced potassium storage performance. *ACS Nano.* 2020;14(10):13938. <https://doi.org/10.1021/acsnano.0c06360>.
- [34] Sarycheva A, Gogotsi Y. Raman spectroscopy analysis of the structure and surface chemistry of Ti₃C₂T_x MXene. *Chem Mater.* 2020;32(8):3480. <https://doi.org/10.1021/acs.chemmater.0c00359>.
- [35] Wang Z, Duan C, Wang D, Dong K, Luo S, Liu Y, Wang Q, Zhang Y, Hao A. BiSb@Bi₂O₃/SbO_x encapsulated in porous carbon as anode materials for sodium/potassium-ion batteries with a high pseudocapacitive contribution. *J Colloid Interface Sci.* 2020;580(15):429. <https://doi.org/10.1016/j.jcis.2020.07.061>.
- [36] Yu J, Meng BC, Wang LJ, Wang Q, Huang WL, Wang XY, Fang Z. Depositing natural stibnite on 3D TiO₂ nanotube array networks as high-performance thin-film anode for lithium-ion batteries. *Rare Met.* 2021;40(11):3215. <https://doi.org/10.1007/s12598-020-01658-0>.

- [37] Tang J, Huang X, Lin T, Qiu T, Huang H, Zhu X, Gu Q, Luo B, Wang L. MXene derived TiS₂ nanosheets for high-rate and long-life sodium-ion capacitors. *Energy Storage Mater.* 2020;26: 550. <https://doi.org/10.1016/j.ensm.2019.11.028>.
- [38] Zhou X, Zhong Y, Yang M, Hu M, Wei J, Zhou Z. Sb nanoparticles decorated N-rich carbon nanosheets as anode materials for sodium ion batteries with superior rate capability and long cycling stability. *Chem Commun (Camb).* 2014; 50(85):12888. <https://doi.org/10.1039/c4cc05989a>.
- [39] Dashairya L, Das D, Saha P. Elucidating the role of graphene and porous carbon coating on nanostructured Sb₂S₃ for superior lithium and sodium storage. *J Alloys Compd.* 2021;883(25): 160906. <https://doi.org/10.1016/j.jallcom.2021.160906>.

Springer Nature or its licensor (e.g. a society or other partner) holds exclusive rights to this article under a publishing agreement with the author(s) or other rightsholder(s); author self-archiving of the accepted manuscript version of this article is solely governed by the terms of such publishing agreement and applicable law.